catalysts

MDPI

Article

Cerium-Doped $CoMn_2O_4$ Spinels as Highly Efficient Bifunctional Electrocatalysts for ORR/OER Reactions

Xiao Chen [1,2], Fengshuang Han [1], Xi Chen [1], Chenxi Zhang [1] and Wangyan Gou [2,*]

[1] School of Materials Science and Engineering, North China University of Water Resources and Electric Power, Zhengzhou 450045, China
[2] Key Laboratory of Special Functional and Smart Polymer Materials of Ministry of Industry and Information Technology, School of Chemistry and Chemical Engineering, Northwestern Polytechnical University, Xi'an 710072, China
* Correspondence: gouwangyan@nwpu.edu.cn

Abstract: Low-cost and highly efficient electrocatalysts for oxygen reactions are highly important for oxygen-related energy storage/conversion devices (e.g., solar fuels, fuel cells, and rechargeable metal-air batteries). In this work, a range of compositionally-tuned cerium-doped $CoMn_2O_4$ (Ce-CMO-X) spinels were prepared via oxidizing precipitation and subsequent crystallization method and evaluated as electrocatalysts for the oxygen reduction reaction (ORR) and oxygen evolution reaction (OER). The Ce modification into the CMO spinels lead to the changes of surface electronic structure. And Ce-CMO-X catalysts display better electrochemical performance than that of pristine CMO spinel. Among them, Ce-CMO-18% shows the best activity. The Ce-CMO-18% processes a higher ratio of Co^{3+}/Co^{2+}, Mn^{4+}/Mn^{3+}, which is beneficial to ORR performance, while the higher content of oxygen vacancies in Ce-CMO-18% make for better OER performance. Thus, the Ce-doped CMO spinels are potential candidates as bifunctional electrocatalysts for both ORR and OER in alkaline environments. Then, the hybrid Ce-CMO-18%/MWCNTs catalyst was also synthesized, which shows further enhanced ORR and OER activities. It displays an ORR onset potential of 0.93 V and potential of 0.84 V at density of 3 mA cm^{-2} (at 1600 rpm), which is comparable to commercial Pt/C. The OER onset potential and potential at a current density 10 mA cm^{-2} are 183 mV and 341 mV. The superior electrical conductivity and oxygen functional groups at the surface of MWCNTs can facilitate the interaction between metal oxides and carbon, which promoted the OER and ORR performances significantly.

Keywords: Ce-doped $CoMn_2O_4$ spinels; oxygen vacancy; oxygen reduction reaction; oxygen evolution reaction

check for updates

Citation: Chen, X.; Han, F.; Chen, X.; Zhang, C.; Gou, W. Cerium-Doped $CoMn_2O_4$ Spinels as Highly Efficient Bifunctional Electrocatalysts for ORR/OER Reactions. *Catalysts* **2022**, *12*, 1122. https://doi.org/10.3390/catal12101122

Academic Editors: Xiangjiu Guan and Shichao Zong

Received: 17 August 2022
Accepted: 23 September 2022
Published: 27 September 2022

Publisher's Note: MDPI stays neutral with regard to jurisdictional claims in published maps and institutional affiliations.

Copyright: © 2022 by the authors. Licensee MDPI, Basel, Switzerland. This article is an open access article distributed under the terms and conditions of the Creative Commons Attribution (CC BY) license (https://creativecommons.org/licenses/by/4.0/).

1. Introduction

With the increasing demands of global energy production and highly negative effects on the environment from fossil fuels, it is expected to develop new technologies to utilize clean and sustainable energy sources [1,2]. Catalytic oxygen reduction/evolution reactions (ORR/OER) are the determinant of various electrochemical energy storage and conversion techniques, including metal–air batteries, fuel cells, and solar or electricity-driven water splitting [3,4]. As for energy conversion devices, both ORR and OER reactions are occurring at same place, which requires that the working electrode has dual functions [5]. However, the sluggish multiple electron transfer process of ORR and OER presents a significant impedance to the practical application, making oxygen electrocatalysts essential for these energy conversion systems [6]. Materials such as platinum group metals (e.g., Pt, Ir) can significantly catalyze these oxygen reactions, thus improving the energy conversion efficiency [7,8]. However, their high cost and scarcity limit their large-scale applications. Thus, the development of cost-effective and high-performance non-noble metal catalysts for OER and ORR plays a vital role. Vast efforts have been made to develop alternative catalysts

based on earth-abundant mixed metals oxides [9], chalcogenides [10], perovskite [11,12], and non-metallic materials [13]. Among them, spinel-typed ($A_xB_yO_z$) complex oxides with controllable composition, chemical valence, morphology, and crystal structure show potential as effective catalysts in ORR/OER reactions [14].

As a typically mixed transition metal spinel, cobalt manganese oxides ($CoMn_2O_4$ or $Co_{3-x}Mn_xO_{4\pm\delta}$) with cubic and tetragonal phases have shown great potential as electrocatalysts, owing to their excellent structural stability and rich redox reactions [15–17]. Previous reports demonstrated that the intrinsic electrocatalytic activity of the CMO family correlates with the crystal phase, Co/Mn composition, and surface valence value, which affect the extent of O_2 activation and the number of available active sites [15,18]. However, these materials generally possess comparably low intrinsic catalytic activity [19]. Many strategies were identified to effectively enhance the reaction activity, including designing unique nano/micro structures, regulating composition by doping hetero-atom dopant, and integrating conductive matrixes [20–22].

Recently, the chemical doping of rare earth elements into electrocatalysts shows their potential to modulate the electronic structures and deliver the improved electrocatalytic activity of ORR and OER reactions [21,23,24]. For example, Long et al. constructed a Ce-doped spinel typed-Co_3O_4 catalyst to enhance the ORR performance [24]. The larger ionic radius and unique 4f electrons orbital of the Ce ion can regulate the geometric and electronic structure of the host lattice [25]. Moreover, the Ce ion has a remarkable redox couple (Ce^{3+}/Ce^{4+}), which improves electron transfer between Ce^{3+}/Ce^{4+} and active sites as well as facilitates the activity of OER and ORR [26,27]. However, a facile method to dope Ce into $CoMn_2O_4$ and the utilization of synergistic effect between Ce and $CoMn_2O_4$ to enhance electrocatalytic performance for OER/ORR has been rarely reported.

Herein, we report that cerium-doped cubic $CoMn_2O_4$ (Ce-CMO-X, X represent the doping content of Ce ions) spinel nanoparticles and hybrid Ce-CMO/MWCNTs (multiple walled carbon nanotubes) nanostructure as high-efficiently bifunctional OER/ORR electrocatalysts, which were fabricated by a facile approach. Firstly, a series of Ce-CMO-X (X = 14%, 18%, 22%) spinel nanoparticles with cubic phase were manufactured via oxidizing precipitation and subsequent crystallization. The electronic structure of CMO was modulated by doping different amounts of Ce, which can efficiently accelerate the catalytic activity and prolong the stability. Benefiting from the metal redox couples (Ce^{3+}/Ce^{4+}) and a higher ratio of surface oxygen content, the as-obtained Ce-CMO-18% showed decent catalytic activity in both ORR and OER. Then, the MWCNTs were induced as the supports of Ce-CMO-18% to form a hybrid Ce-CMO-18%/MWCNTs nanostructure, which displays an OER onset potential of 0.93 V and potential of 0.84 V at a current density of 3 mA cm^{-2} (at 1600 rpm). The OER onset potential and potential at 10 mA cm^{-2} of Ce-CMO-18%/MWCNTs are 183 and 341 mV, which further enhanced both OER and ORR catalytic activities. In this work, the effect of Ce-doping in cubic $CoMn_2O_4$ spinels on OER/ORR was studied, which provides a promising method to build bifunctional catalysts.

2. Results and Discussion

2.1. Synthesis and Characterizations of $CoMn_2O_4$ (CMO) and Ce-CMO-X Electrocatalysts

The typical synthetic route to Ce-CMO-X (X = 14%, 18%, 22%) spinel nanoparticles involve oxidizing precipitation of Ce/Mn/Co salts with $NH_3 \cdot H_2O$ under air atmosphere and subsequent crystallization into spinel at mild temperature (180 °C). According to the actual mass content of the Ce element which identified by ICP results (Table S1), three kinds of Ce-CMO-X spinels are denoted as Ce-CMO-14%, Ce-CMO-18%, and Ce-CMO-22%. The morphology and elemental distribution of the as-obtained CMO and Ce-CMO-X were characterized by using transmission electron microscopy (TEM), high-resolution transmission electron microscopy (HRTEM), and elemental dispersive spectrometer (EDS)-mapping analysis as shown in Figure 1. Revealed from TEM images (Figures 1a,d and S1), the morphological features of Ce-CMO-X at various doping levels are basically similar to the pristine CMO nanoparticles. Figure 1b shows the HRTEM image of CMO nanoparticles,

where the interplanar distances of 0.26 and 0.29 nm correspond to the $(\bar{1}3\bar{1})$ and (220) crystalline planes, respectively, similar to the previous report. The pristine CMO possesses a spinel structure with a close-packed face-centered cubic (fcc) configuration of O^{2-} ions, where Mn^{3+} ions occupy the centers of octahedrally coordinated positions while Co^{2+} ions occupy the tetrahedral sites [14]. After chemical doping of cerium ion into CMO nanoparticles, the interplanar space of the (220) crystalline plane was increased to 0.30 nm (Figures 1e and S1b,d), which could be attributed to the bigger ionic radius of cerium than cobalt and manganese ions. The crystal structures of CMO and Ce-CMO-X were analyzed by XRD (Figure 1c). Reflection peaks of all electrocatalysts can be assigned to the space group of Fd-3m, consistent with the standard pattern of the fcc spinel phase (JCPDS card no. 23-1237). For all Ce-CMO-X electrocatalysts, characteristic XRD peaks of CeO_2 were not observed, suggesting the successfully chemical doping. Furthermore, HAADF-STEM images and the corresponding EDS mappings of Ce-CMO-18% (Figures 1f and S2) show the uniform distribution of Mn, Ce, and Co elements, confirming a clear presence and uniform distribution of Ce element in the CMO lattice structure.

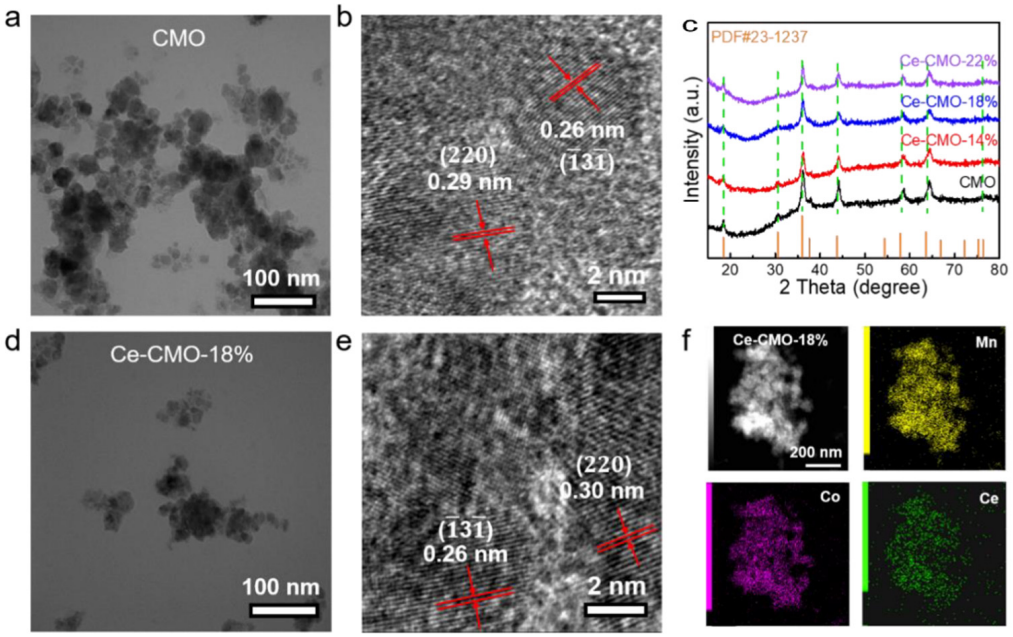


Figure 1. The characterization of catalysts: (**a**) TEM image and (**b**) HRTEM image of CMO nanoparticles; (**c**) XRD patterns of CMO nanoparticles and various Ce-CMO-X nanoparticles; (**d**) TEM image and (**e**) HRTEM image of Ce-CMO-18%; (**f**) HAADF-STEM image and the corresponding EDS mapping of Ce-CMO-18%.

Vibrational spectroscopy can observe the minor quantity of impurity and lattice distortions. Thus, Raman measurements were also conducted on pristine CMO and Ce-CMO-X nanoparticles (Figure S3). The characteristic Raman peaks of CeO_2 at ~460 cm^{-1} (triply degenerate F_{2g} mode of CeO_2) were absent in all Ce-CMO-X catalysts, further confirming the successfully Ce-chemical doping and consistent with the results of XRD (Figure 1c) [28]. In the high-frequency region of Raman spectra, a high frequency band peaks at 554 cm^{-1} and a broader band at a higher frequency (620–650 cm^{-1}) can be assigned to the vibrational modes of the MnO_6 octahedral. In the view of the stretching mode frequency decreases, partial Mn-O bond length increases, which qualitatively owing to the doping of the cerium ion into the lattice of CMO spinel nanoparticles, the stretching mode frequency decreases [29]. Also, the broadening of the modes of MO_6 octahedral after Ce doping was also observed, which could be attributed to a disorder of the structure induced by the intercalation of guest Ce atoms. BET (Brunner–Emmet–Teller) surface areas were obtained from N_2 adsorption/desorption isotherms. The BET surface areas of 31.4, 30.9, 38.7, and 31.1 $m^2\ g^{-1}$ were obtained from CMO, Ce-CMO-14%, Ce-CMO-18%, and

Ce-CMO-22%, respectively (Figure S4a). Furthermore, the pore size distribution plots were shown in Figure S4b, which indicated the presence of mesopores in all samples. The BJH adsorption average pore diameters were 16.9, 22.1, 19.7, and 26.3 nm for CMO, Ce-CMO-14%, Ce-CMO-18%, and Ce-CMO-22%, respectively. The above results all suggested that Ce-CMO-X samples were fabricated successfully.

2.2. The Electronic Structure of CMO Spinels after Ce Doping

To obtain detailed information about the elemental character and oxidation state of the as-prepared CMO and Ce-CMO-X samples, X-ray photoelectron spectra (XPS) measurements were performed. An elemental survey of XPS indicates the presence of Co, Mn, Ce, and O elements in Ce-CMO-X spinels (Figure S5), consistent with element mapping results. Figure 2 and Table 1 present the XPS fine spectra and valence state distribution of Co 2p, O 1s, and Ce 3d profiles. As displayed in Figure 2a, the Co 2p XPS spectra show two split spin-orbit components, namely, Co $2p_{3/2}$ and Co $2p_{1/2}$. The peaks at 797 and 782 eV belong to Co^{2+}, while the peaks with binding energies at 795 and 780 are ascribed to Co^{3+} and two shakeup satellites peaks centered at 787 and 803 eV, indicating the coexistence of Co^{2+} and Co^{3+} [27]. As shown in Table 1, the ratio of Co^{3+}/Co^{2+} increased after incorporating the Ce element. When the Ce doping amount reaches 18%, the ratio of Co^{3+}/Co^{2+} reaches the maximum value of 0.96, which is obviously bigger than that of the initial CMO (0.67). Since Co^{3+} ions could act as electron donors and/or acceptors during ORR, that ORR process is assumed to take place at the active sites where Co^{3+} ions present a higher oxidation state in the Co-based catalysts [30].

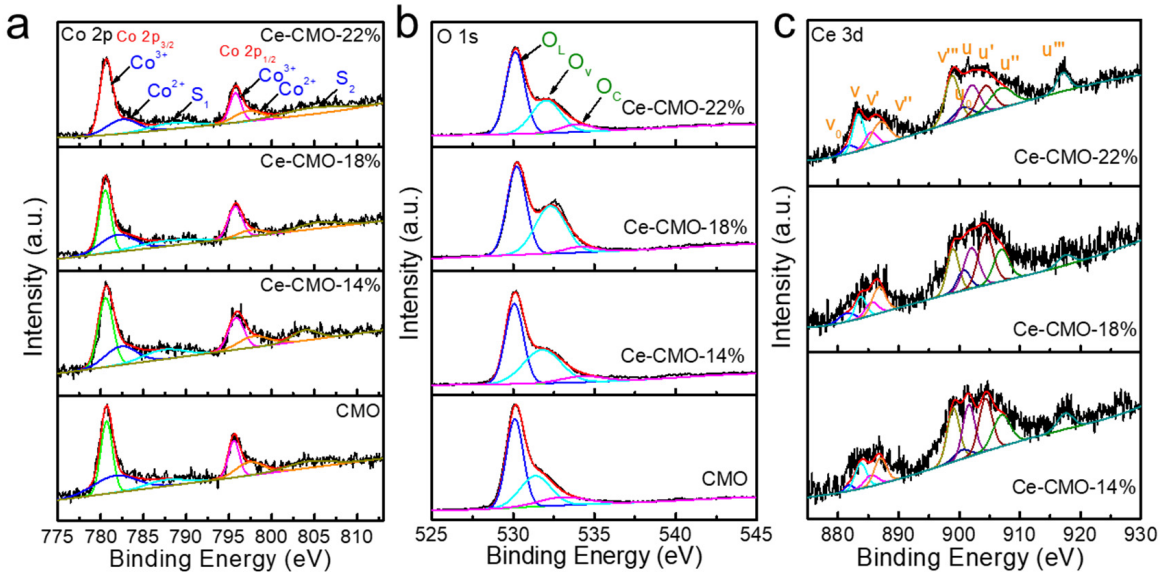


Figure 2. The XPS spectra of CMO, Ce-CMO-14%, Ce-CMO-18%, and Ce-CMO-22% electrocatalysts: (**a**) Co 2p, (**b**) O 1s, and (**c**) Ce 3d.

Table 1. The valence state distribution of Co 2p, O 1s, Ce 3d, and Mn 2p.

Sample	Co 2p (Co^{3+}/Co^{2+})	O 1s (O_V/O_L)	Ce 3d (Ce^{3+}/Ce^{4+})	Mn 2p (Mn^{4+}/Mn^{3+})
CMO	0.67	0.62	-	0.39
Ce-CMO-14%	0.72	0.75	0.41	0.49
Ce-CMO-18%	0.96	0.85	0.56	0.54
Ce-CMO-22%	0.70	0.70	0.34	0.42
Ce-CMO-18%/MWCNTs	1.01	1.10	0.45	0.53

Moreover, the Mn 2p spectra of the pristine CMO and Ce-CMO-X spinel nanoparticles can be fitted with two pairs of spin-orbit deconvoluted peaks ascribing to the oxidation states of Mn^{3+} and Mn^{4+} (Figure S6), indicating the presence of multiple valences of Mn on the oxide surface. The chemical doping of Ce into the lattice of CMO caused an enhanced ratio of Mn^{4+} to Mn^{3+}. Jahn Teller effect can be raised from Mn^{3+} occupying the octahedral site, reducing the crystallographic symmetry of the cubic phase of CMO spinels [15]. Previous research demonstrated that the Jahn Teller effect reduces the oxygen adsorbate ability [18]. Thus, a higher proportion of Mn^{4+} with a suppressed Jahn Teller effect might efficiently facilitate the activity of oxygen-involved reaction [31].

Figure 2b displays the high-resolution O 1s spectra of CMO and Ce-CMO-X catalysts. The deconvolution of O 1s spectra shows three peaks located at ~530, ~532, and ~534 eV for all samples, corresponding to the lattice oxygen species (O_L), surface oxygen vacancy (O_V), and chemisorbed oxygen (O_C), respectively [32]. The concentration of O_V on the spinel catalyst can be evaluated by the following Equation (1) [33]:

$$O_V\% = \frac{A_{O_V}}{A_{O_L} + A_{O_V} + A_{O_C}} \times 100\% \quad (1)$$

With the addition of Ce in the CMO lattice structure, the relative concentration of surface oxygen in Ce-CMO-X (X = 14%, 42%; X = 18%, 43%; X = 22%, 34%) is higher than that in pristine CMO (33%), indicating doping Ce is an effective strategy to engineering more O_V. Figure 2c shows the Ce 3d XPS spectra of Ce-CMO-X catalysts. The deconvoluted v_0, v', u_0, and u' peaks can be assigned to Ce^{3+}, while v, v″, v‴, u, u″, u‴ belong to Ce^{4+} [31]. Notably, compared with Ce-CMO-14% (0.41) and Ce-CMO-22% (0.34), Ce-CMO-18% (0.56) possess the highest ratio of Ce^{3+}/Ce^{4+}. It is believed that the Ce^{3+} concentration is a key factor that determines the oxygen vacancies assorted in the catalysts. The feasibility and enhancement of the Ce^{3+}/Ce^{4+} redox transition rely on the oxygen vacancy density [34]. To further investigate the intrinsic defects of the pristine CMO and Ce-CMO-18% catalysts, we analyzed electron paramagnetic resonance (EPR) spectra to probe the existence of oxygen vacancy defects for the catalyst materials [35]. As shown in Figure S7, the enhanced signal intensity at g = 2.001 illustrates that the Ce-CMO-18% processes more oxygen vacancies when doping Ce^{3+} into CMO. Such richness in O_V can be attributed to the high and flexible coordination number of cerium ions that alters the topology of the layer and brings about lattice distortion and laminar imperfections [26].

Previous investigations have demonstrated that Co^{3+} and Mn^{4+} species are beneficial for the ORR process [36]. Furthermore, the higher proportion of Ce^{3+} and O_V in Ce-CMO-X also potentially benefits better OER activity [37]. Thus, the chemical doping of cerium in CMO spinel catalysts effectively modulates the electronic structures of the surface-active species and achieves higher OER and ORR activity as a consequence.

2.3. OER and ORR Performance of CMO and Ce-CMO Electrocatalysts

The correlation between Ce contents in these CMO and Ce-CMO-X catalysts prepared at different Ce/Co ratios (Ce/Co = 0%, 14%, 18%, 22%) and their electrocatalytic activity for the OER was explored by using a standard three-electrode system in 1 M KOH solution at room temperature (Figure 3). The pristine CMO and Ce-CMO-X electrocatalysts were deposited onto a piece of carbon fiber paper with the same total weight density of 0.56 mg cm^{-2}. *iR*-corrected linear sweep voltammetry (LSV) polarization curves indicated that all of the Ce-CMO-X catalysts exhibited higher OER performance than the pristine CMO catalysts. Thus, the introduction of Ce ion in the host lattice of CMO significantly improved their electrocatalytic activity (Figure 3a). Among them, the Ce-CMO-18% electrocatalysts delivered the best OER performance with an onset potential of 378 mV and overpotential of 476 mV at a current density of 10 mA cm^{-2} (Figure 3a and Table 2). In contrast, the pristine CMO catalysts presented a much larger onset potential of 414 mV and overpotential of 562 mV to reach a catalytic current density of 10 mA cm^{-2}. The Tafel slopes decreased from 138 mV dec^{-1} of CMO to 86 mV dec^{-1} of Ce-CMO-18%, as shown in

Figure 3b and Table 2, suggesting the significantly accelerated reaction kinetics and higher electrocatalytic activity of the Ce-CMO-18%.

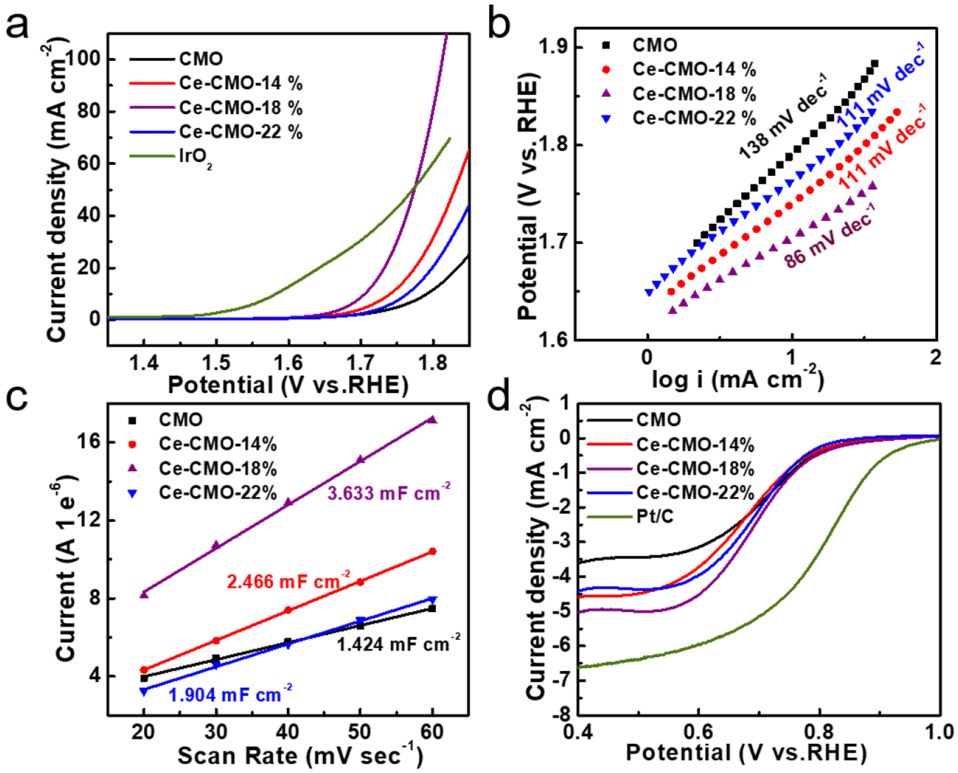


Figure 3. The OER and ORR properties of CMO and Ce-CMO-X electrocatalysts: (**a**) The undistorted *iR*-corrected LSV polarization curves in 1 M aqueous KOH at 10 mV s^{-1} and (**b**) Tafel plots; (**c**) ECSA plots; (**d**) LSV polarization curves of the ORR in O_2-saturated 0.1 M KOH solution at 1600 rpm.

Table 2. The OER and ORR performance of CMO and Ce-CMO-X electrocatalysts.

Sample	OER			ORR	
	η_{onset} (mV)	η (mV) @ 10 mA cm^{-2}	Tafel slope (mV dec^{-1})	J_L (mA cm^{-2})	E (mV) @ 3 mA cm^{-2}
CMO	414	562	138	3.4	617
Ce-CMO-14%	398	511	111	4.5	643
Ce-CMO-18%	378	476	86	5.0	675
Ce-CMO-22%	419	534	111	4.4	660

To further understand their OER activity, the electrochemically active surface area (ECSA) of the electrocatalysts was estimated by CV (cyclic voltammetry). The double layer capacitance (C_{dl}) of the catalysts was calculated, which was proportional to ECSA (Figure S8). As observed in Figure 3c, ECSA was raised in Ce-CMO-X catalysts, which could be attributed to partial lattice expansion and, consequently, more exposed active sites. Specifically, the ECSA of Ce-CMO-18% increased nearly 2.5 times higher than that of the pristine CMO nanoparticles (Figure 3c). The EIS technique was also applied to measure the charge transfer resistance (R_{ct}) of the samples. Figure S9a shows the Nyquist plots with the smallest semicircle diameter for the Ce-CMO-18%. Table S2 listed the solution resistance (R_s) and R_{ct} values of different samples. The R_{ct} value of Ce-CMO-18% was found to be 190.2 Ω, lower than that of CMO (362.6 Ω), Ce-CMO-14% (207.0 Ω), and Ce-CMO-22% (253.4 Ω), indicating its rapid charge transfer ability [38]. To further estimate the intrinsic catalytic activity of the different catalysts, the turnover frequency (TOF) was calculated to obtain the rate of oxygen generation to the number of active sites of the catalyst by the

CV tests shown in Figure S10a. Figure S10b indicated that the Ce-CMO-18% possesses a better TOF behavior as compared with pristine CMO, Ce-CMO-14%, and Ce-CMO-22%. The TOF value of the electrocatalysts for OER at an overpotential of 0.46 V was in the order of Ce-CMO-18% (3.21 s^{-1}) > Ce-CMO-14% (1.92 s^{-1}) > CMO (1.21 s^{-1}) > Ce-CMO-22% (1.15 s^{-1}) respectively. Thus, showing the better intrinsic OER catalytic activity for the Ce-CMO-18%.

Then, the electrocatalytic ORR activity of pristine CMO spinel nanoparticles and Ce-CMO-X nanoparticles was also evaluated at a glass carbon electrode in 0.1 M KOH solution, as shown in Figure 3d and Table 2. From the polarization curves with a rotating rate of 1600 rpm, it is worth noting that although all catalysts show similar ORR onset potential (0.83 V), the higher current density demonstrates Ce-CMO-X show decent ORR activity with higher current density. The Ce-CMO-18% shows the most positive potential (0.68 V) at a current density of 3 mA cm^{-2}, higher than that of pristine CMO (0.62 V).

Based on the above results, both ORR and OER activities of Ce-CMO-18% are obviously higher than that of other catalysts. The ORR catalytic performance followed an order of Ce-CMO-18% > Ce-CMO-22% > Ce-CMO-14% > CMO, and the OER activity followed an order of Ce-CMO-18% > Ce-CMO-14% > Ce-CMO-22% > CMO, respectively. Combining the surface electronic structure of electrocatalysts with their catalytic activities, the better OER and ORR performance of Ce-doped CMO spinels nanoparticles can be ascribed to these factors: (1) the disorder of the Ce-doped CMO spinel structure and thus more exposed active sites on the surface, (2) more generated surface oxygen species resulting from the introduction of Ce elements, (3) the modulation of the electronic structure of Co and Mn ions to form more Co^{3+} and Mn^{4+}, and the resulted enhancement of the adsorption of oxygen intermediates and suppression the Jahn Teller effect.

2.4. Bifunctional OER and ORR Catalytic Performance of Ce-CMO-18%/MWCNTs

To further improve the electrocatalytic performance of the Ce-CMO-18% spinel nanoparticles, MWCNTs with high conductivity and special chemical properties were also added during the synthetic process of the Ce-CMO-18% spinel nanoparticles. Herein, the Ce-CMO-18% electrocatalysts with the best OER and ORR activity were chosen to study the benefits of MWCNTs for their electrocatalytic properties. In the Raman spectra of MWCNTs and Ce-CMO-18%/MWCNTs (Figure 4a), the peaks at ~1270, ~1590, and ~2540 cm^{-1} correspond to the D band, G band, and the second order G' band of typical MWCNTs, indicating the presence of MWCNTs in the electrocatalysts. Figure 4b,c show the TEM image and HRTEM micrographs of Ce-CMO-18%/MWCNTs, which indicates that the particles of Ce-CMO-18% were grown on the surface of MWCNTs to form a hybrid structure. The phase of Ce-CMO-18% spinel nanoparticles was maintained in the composites from XRD patterns (Figure S11).

The chemical environment of the Ce-CMO-18%/MWCNTs were further investigated by XPS. Figure S12a–d shows the fine spectrum of Co 2p, O 1s, Ce 3d, and Mn 2p. Compared to Ce-CMO-18%, XPS results suggest that Ce-CMO-18%/MWCNTs with higher content of Co^{3+} and O_S, while the ratio of Mn^{4+}/Mn^{3+} and Ce^{3+}/Ce^{4+} were slightly decreased (Figure S12e). These results indicate the presence of multiple valences of Co, Mn, and Ce elements on the oxide surface. Furthermore, many oxygenic functional groups on the surface of MWCNTs, facilitate the interaction between metal oxides and carbon [34]. Therefore, the intimate hybridization interaction renders the nanocomposite highly conductive and electrochemical active, favoring the enhancement of electrocatalytic capability [39].

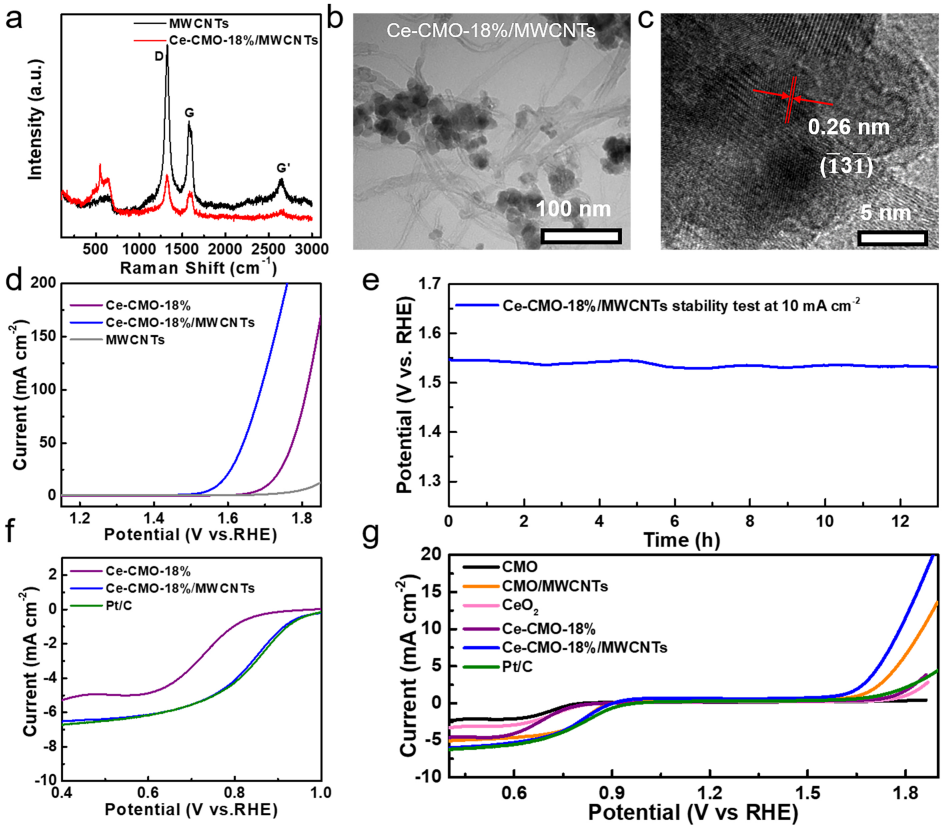


Figure 4. (**a**) Raman spectra of MWCNTs and Ce-CMO-18%/MWCNTs; (**b**) TEM image and (**c**) HRTEM image of Ce-CMO-18%/MWCNTs; (**d**) the OER LSV polarization curves in 1 M aqueous KOH at 10 mV s^{-1}; (**e**) long-term chronopotentiometric curve test of Ce-CMO-18%/MWCNTs at a current density of 10 mA cm^{-2}; (**f**) ORR LSV polarization curves of CMO, Ce-CMO-18%, Ce-CMO-18%/MWCNTs, and Pt/C in O_2-saturated 0.1 M KOH solution at 1600 rpm; (**g**) total LSV curves of the as-obtained samples in the ORR and OER processes.

As shown in Figure 4d, the Ce-CMO-18%/MWCNTs electrocatalysts exhibit the lowest onset potential (183 mV) and overpotential (341 mV, 10 mA cm^{-2}) among the studied catalysts, while the bare MWCNTs deliver negligible OER activity. The Tafel slopes of these electrocatalysts were shown in Figure S13, which revealed that Ce-CMO-18%/MWCNTs show similar Tafel slopes (84 mV dec^{-1}) with Ce-CMO-18%, confirming the presence of MWCNTs in catalysts, improved the OER activity on the basis of unchanged RDS. The Nyquist diagram of Ce-CMO-18%/MWCNTs and R_{ct} were shown in Figure S9b and Table S2, the lower R_{ct} (66.8 Ω) than that of Ce-CMO-18% (190.2 Ω) suggested that the better charge transport ability, which further identified the benefits of the combination of MWCNTs. Figure 4e shows good OER durability of Ce-CMO-18%/MWCNTs. As shown in Figure S14, the TOF value of Ce-CMO-18%/MWCNTs (3.97 s^{-1} at an overpotential of 0.34 V) was also calculated, indicating the better OER activity than Ce-CMO-18%. The operating overpotential for the Ce-CMO-18%/MWCNTs is nearly constant after 13 h of testing. Meanwhile, after the stability test, TEM and XPS analyses were conducted. The TEM image of Ce-CMO-18%/MWCNTs after OER studies is shown in Figure S15. The image shows the complete morphological retention of Ce-CMO-18%/MWCNTs catalysts. XPS spectra after OER indicate that Co 2p, Mn 2p, and Ce 3d still show their characteristic peaks in Ce-CMO-18%/MWCNTs (Figure S16). As shown in Figure S17, the high-resolution of O 1s spectra for used-Ce-CMO-18%/MWCNTs reveals the obviously increasing content of O_S, meaning that the lattice oxygen oxidation during the OER process, which is beneficial for the OER activity [31]. The peak at a binding energy of 535 eV attributed to O-S bond was originated from the Nafion solution [40].

Then, the ORR activities of these obtained samples were tested by using a rotating disk electrode (RDE) in 0.1 M KOH electrolyte at a rotation rate of 1600 rpm. Firstly, CV of pristine CMO, Ce-CMO-18%, and Ce-CMO-18%/MWCNTs catalysts was tested in O_2- and Ar-saturated 0.1 M KOH solution. As shown in Figure S18, no obvious redox peaks were observed in the CV data collected under the Ar atmosphere. Therefore, the reduction peaks of the voltammograms in O_2-saturated solution can be ascribed to the reduction reaction of O_2 only. Figure 4f displays the ORR LSV curves. The Ce-CMO-18%/MWCNTs composites exhibited an onset potential at 0.93 V and potential of 0.84 V at a current density of 3 mA cm^{-2}, which is comparable to commercial Pt/C (0.85 V, 3 mA cm^{-2}). After that, the polarization curves with different rotation rates (900–2500 rpm) and the corresponding Koutecky–Levich (K-L) plots of Ce-CMO-18%/MWCNTs composites are shown in Figure S19. The K–L plots exhibit good linearity, and the slopes remain constant over a wide potential range (0.4–0.7 V), thus suggesting consistent electron transfer for the oxygen reduction reaction. Based on the slopes, the electron transfer number (n) is calculated as ~4. It is evident that the ORR process catalyzed by the Ce-CMO-18%/MWCNTs proceeds via an almost highly favorable one-step four-electron reduction.

Furthermore, the ORR stability of Ce-CMO-18%/MWCNTs and commercial Pt/C were tested by using chronoamperometry at an applied potential of 0.75 V (Figure S20). Figure S16 shows the current density of the Ce-CMO-18%/MWCNTs can be maintained 90.3% after 9 h at 0.4 V, while the Pt/C only maintains 50%. The negligible decay of current density during measurements indicated the high catalytic stability of the Ce-CMO-18%/MWCNTs composites. Besides, the significant improvement of methanol tolerance was realized by Ce-CMO-18%/MWCNTs, as shown in Figure S21. Finally, the overall LSV curves of different catalysts were tested at a rotation rate of 1600 rpm in O_2-saturated 0.1 M KOH (Figure 4g). The pristine CMO and CeO_2 show poor ORR/OER catalytic activity, which suggests that the doping of Ce element into CMO distinct improve the reaction activity. As for Ce-CMO-18% and Ce-CMO-18%/MWCNTs catalysts, the adding of MWCNTs further enhanced ORR and OER activities. Compared with commercial Pt/C catalysts, Ce-CMO-18%/MWCNTs shows comparable ORR performance and better OER activities. All of these tests indicate that the Ce-CMO-18%/MWCNTs composites deliver good stability and activity in alkaline solutions both in ORR and OER processes.

3. Materials and Methods

3.1. Materials

Cobalt(II) nitrate hexahydrate ($Co(NO_3)_2{\cdot}6H_2O$, Energy Chemical, 98%), Manganese(II) nitrate tetrahydrate ($Mn(NO_3)_2{\cdot}4H_2O$, Energy Chemical, Shanghai and China 98%), Cerium(III) nitrate hexahydrate ($Ce(NO_3)_3{\cdot}6H_2O$, Energy Chemical, Shanghai and China 99.99%), Ammonium hydroxide ($NH_3{\cdot}H_2O$, Energy Chemical, Shanghai and China AR, 28.0–30.0% NH_3), Nafion (Sigma-Aldrich, Shanghai and China ~5% in a mixture of lower aliphatic alcohols and water). All chemicals used in the experiments are analytical grade and without further purification.

3.2. Experimental Section

3.2.1. Synthesis of CMO and Ce-CMO-X Nanoparticles

In a typical synthesis of $CoMn_2O_4$ spinel nanoparticles, 2 mL of aqueous ammonia (25–28 wt%) was dropped into 2.5 mL of 0.2 M $Co(NO_3)_2$ aqueous solution under the constant stirring in a crucible at room temperature. Then, 5 mL of 0.2 M $Mn(NO_3)_2$ aqueous solution was added to the above mixture. After 2 h stirring, the mixture was heated at 180 °C for 2 h to evaporate water and decompose nitrates, yielding the $CoMn_2O_4$ spinel nanoparticles. The Ce-CMO-X nanoparticles were obtained in a similar approach with the addition of various amounts of $Ce(NO_3)_3$ in 0.2 M $Mn(NO_3)_2$ aqueous solution. The electrocatalysts were dried at 60 °C and stored for future use. The obtained samples were named CMO, Ce-CMO-14%, Ce-CMO-18%, and Ce-CMO-22%, which correspond to 0, 0.05, 0.075, and 0.1 mmol of cerium nitrate, and were added during the synthesis, respectively. A

total of 14%, 18%, and 22% represent the actual mass percent of Ce in every sample, which was identified by ICP results.

3.2.2. Synthesis of Ce-CMO-18%/MWCNTs Composites

Initially, the pristine MWCNTs were annealed at 500 °C for 10 min in a tube furnace in the air to remove amorphous carbon. Then, the thermally treated MWCNTs were stirred in the concentrated HCl and HNO_3 (v/v = 3:1) mixed solution for 30 min at room temperature to dissolve the residual metal components. The purified MWCNTs were filtered through a 0.45-μm filter, washed with deionized water until the pH reached 7, and dried in an electric oven at 60 °C. Synthesis of the Ce-CMO-18%/MWCNTs composites was through a similar procedure of Ce-CMO-18%, in which 25 mg of the purified MWCNTs was dispersed in 2.5 mL of 0.2 M $Co(NO_3)_2$ aqueous solution.

3.3. Characterization

X-ray diffraction (SMARTLAB (3), Kyoto, Japan) measurements were performed on a Shimadzu X-ray diffractometer using Cu Kα radiation. The Ce content was determined by PerkinElmer Optima 2100 DV (Shelton CT, USA) inductively coupled plasma optical emission spectrometer (ICP-OES) analysis. Raman spectra were collected from a Horiba JOBIN YVON Raman spectrometer using a 633 nm laser device. Transmission electron microscopy (TEM, Kyoto, Japan) studies were conducted on a Hitachi HT-7700 transmission electron microscope with an accelerating voltage of 120 kV. High-resolution TEM images were performed on an FEI Tecnai G2 F20 S-Twin microscope with an accelerating voltage of 200 kV. High-angle annular dark field (HAADF) scanning TEM (STEM) images and the corresponding energy-dispersive X-ray spectroscopy (EDS, Jean, Germany) mappings were analyzed by a ZEISS MERLIN Compact and Oxford x-max operated at an acceleration voltage of 30.0 kV. X-ray photoelectron spectra (XPS, Boston MA, USA) were acquired on a Thermo Electron Model K-Alpha with Al Kα as the excitation source. Thermogravimetric analysis (TGA, Zurich, Switzerland) of as-synthesized samples was carried out at Mettler Toledo, STARe, at a heating rate of 5 °C min^{-1} from room temperature to 800 °C in air. The Brunauer–Emmett–Teller (BET, Norcross, GA, USA) specific surface area was determined using N_2 adsorption-desorption on the TriStarII3020 system (micromeritics). Electron paramagnetic resonance (EPR, Card in bielefeld, Germany) spectra were performed on Bruker EMX PLUS to identify the presence of oxygen vacancies in the samples. The testing parameters were as follows: microwave frequency of 9.2996 GHz, microwave power at 6.325 mW, sweep time of 30 s.

3.4. Electrochemical Measurements

The catalyst ink was prepared by dispersing 4 mg of catalyst in a mixed solvent containing 768 μL of H_2O, 200 μL of EtOH, and 32 μL of 5 wt% Nafion. Then, 10 μL of the catalyst ink (containing 40 μg of the catalyst) was loaded onto a carbon fiber paper (CFP) (0.56 mg/cm^2). Electrochemical measurements were carried out on a CHI 660D electrochemistry workstation (CH Instrument, Shanghai, China), including linear sweep voltammograms (LSV) and current voltammograms (CV). OER electrocatalytic performances were evaluated in a three-electrode system and in 1 M KOH aqueous solution with catalysts/CFP, Pt wire, and the saturated calomel electrode (SCE) used as the working electrode, the counter electrode, and the reference electrode, respectively. The OER durability was determined by the chronopotentiometry tests at a current density of 10 mA cm^{-2}. The EIS measurement was performed at the voltage frequency ranging from 10^5 to 10^{-1} Hz and the applied potential of 1.7 V (vs. RHE). All measured potentials versus Hg/Hg_2Cl_2 were converted to the reversible hydrogen electrode (RHE) scale via the Nernst equation:

$$E_{RHE} = E_{Hg2Cl2} + 0.059\ V \times pH + 0.2412\ V \quad (2)$$

where E_{RHE} is the converted potential versus RHE, E_{Hg2Cl2} is the experimental measured potential against the SCE reference electrode, and 0.2412 V is the saturated potential of Hg/Hg_2Cl_2 at 25 °C.

For the ORR measurements, 1.2 mg of catalysts and 2.8 mg of carbon powder (Vulcan XC-72) were dispersed in a solvent containing 768 µL of H_2O, 200 µL of EtOH, and 32 µL Nafion solution. A total of 4 mg of Ce-CMO-18%/MWCNTs composites can be used directly to prepare the catalyst ink. After thorough sonication, 3 µL of the catalyst ink was pipetted on the glassy carbon electrode (3 mm), which was air-dried to afford a mass loading of 0.051 mg/cm^2. The CV curves were collected after purging O_2 for 30 min at a potential sweep rate of 10 mV s^{-1} in 0.1 M KOH electrolyte. The LSV curves were collected at a sweep rate of 10 mV s^{-1} at 1600 rpm in the O_2-saturated electrolyte conducted on an RDE electrode system. The K–L plots are determined using the K–L equation as follows [14]:

$$\frac{1}{J} = \frac{1}{J_K} + \frac{1}{J_L} = \frac{1}{nFkC_0} + \frac{1}{0.62nFC_0(D_0)^{2/3}v^{-1/6}\omega^{1/2}} \quad (3)$$

where J is the measured current density (mA cm^{-2}), J_k and J_d are the kinetic and diffusion-limiting current densities (mA cm^{-2}), respectively, n is the overall number of electrons transferred, F is the Faraday constant, k is the electron transfer rate constant, C_0 is the O_2 concentration in the electrolyte, D_0 is the diffusion coefficient of O_2 in the electrolyte, v is the viscosity of the electrolyte, and ω is the angular velocity in units of rad s^{-1}.

4. Conclusions

In summary, we reported a simple method to synthesize a series of Ce-doped CMO spinels as bifunctional catalysts for ORR and OER processes. The surface electronic structure of Ce-CMO-X (X = 14%, 18%, 22%) catalysts can be tuned by facile adjusting the amount of Ce content. Results indicated that the addition of Ce elements benefited the ORR/OER activity compared to pristine CMO spinels. Among them, Ce-CMO-18% exhibited the best ORR/OER performance. The enhancement of catalytic activity could be described in terms of the chemical surface and specific surface area. Ce-CMO-18% catalyst with a higher ratio of Co^{3+}/Co^{2+}, Mn^{4+}/Mn^{3+}, and $O_V/O_{L,}$ as well as the larger specific surface area, and suppressed the Jahn–Teller effect, which enhanced the ability to absorb oxygen and expose more active sites, benefitting to the ORR and OER activity. In order to further promote the catalytic activity, MWCNTs were introduced to the Ce-CMO-18% spinels to form Ce-CMO-18%/MWCNTs hybrid. The superior electrical conductivity and oxygen functional groups at the surface of MWCNTs can facilitate the interaction between metal oxides and carbon, which promoted the OER and ORR performances significantly.

Supplementary Materials: The following are available online at https://www.mdpi.com/article/10.3390/catal12101122/s1, Table S1: The ICP results of Ce-CMO-X. Table S2: The EIS results of CMO, Ce-CMO-X, And Ce-CMO-18%/MWCNTs. Figure S1: The characterization of catalysts, Figure S2: The existence of Co, Mn, and Ce elements in Ce-CMO-18% according to EDS mapping. Figure S3: The Raman spectrum of pristine CMO, Ce-CMO-14%, Ce-CMO-18%, and Ce-CMO-22%. Figure S4: (a) N_2 adsorption-desorption isotherms and (b) pore diameter distributions of pristine CMO, Ce-CMO-14%, Ce-CMO-18%, and Ce-CMO-22%. Figure S5: The elemental survey of XPS of pristine CMO, Ce-CMO-14%, Ce-CMO-18%, and Ce-CMO-22%. Figure S6: The Mn 2p spectra of pristine CMO, Ce-CMO-14%, Ce-CMO-18%, and Ce-CMO-22%. Figure S7: The EPR spectrum of CMO and Ce-CMO-18%. Figure S8: The cyclic voltammograms of (a) pristine CMO, (b) Ce-CMO-14%, (c) Ce-CMO-18%, and (d) Ce-CMO-22% at various scan rates (20-60 mV s^{-1}). Figure S9: The Nyquist diagrams of (a) CMO, Ce-CMO-14%, Ce-CMO-18%, Ce-CMO-22%, and (b) Ce-CMO-18%/MWCNTs. Figure S10: (a) CV curves of CMO, Ce-CMO-14%, Ce-CMO-18%, and Ce-CMO-22%, in PBS solution (pH = 7.0) at a scan rate of 50 mV s^{-1}, (b) Calculated O_2 TOF values of CMO, Ce-CMO-14%, Ce-CMO-18%, and Ce-CMO-22%. Figure S11: The XRD patterns of Ce-CMO-18% and Ce-CMO-18%/MWCNTs. Figure S12: The XPS spectra of Ce-CMO-18%/MWCNTs. Figure S13: The corresponding Tafel plots of Ce-CMO-18%, Ce-CMO-18%/MWCNTs, and MWCNTs. Figure S14: (a) CV curves of

Ce-CMO-18%/MWCNTs in PBS solution (pH = 7.0) at a scan rate of 50 mV s^{-1}, (b) Calculated O_2 TOF values of Ce-CMO-18%/MWCNTs. Figure S15: TEM image of the Ce-CMO-18%/MWCNTs after OER durability test. Figure S16: XPS spectra of the Ce-CMO-18%/MWCNTs before and after OER durability test. Figure S17: O 1s XPS spectra of the Ce-CMO-18%/MWCNTs before and after OER durability test. Figure S18: The cyclic voltammograms curves of (a) CMO, (b) Ce-CMO-18%, and (c) Ce-CMO-18%/MWCNTs in Ar- and O_2-saturated 1 M KOH aqueous solution. Figure S19: (a) Oxygen reduction polarization curves for Ce-CMO-18%/MWCNTs at 0.1 M KOH at various rotations rates; (b) Koutecky-Levich plots at different potentials (0.4, 0.5, 0.6, and o.7 V vs. RHE) at a scan rate of 10 mV s^{-1}. Figure S20: The chronoamperometry responses obtained on Pt/C and Ce-CMO-18%/MWCNTs at potential of 0.75 V. Figure S21: *i-t* chronoamperometric response for Pt/C and Ce-CMO-18%/MWCNTs in O_2-saturated 0.1 M KOH solution with addition of methanol at 100 seconds [41,42].

Author Contributions: Conceptualization, W.G.; methodology, X.C. (Xiao Chen) and W.G.; investigation, X.C. (Xiao Chen); resources, W.G.; writing-original draft preparation, X.C. (Xiao Chen), F.H. and X.C. (Xi Chen); writing-review and editing supervision, X.C. (Xiao Chen); W.G., X.C. (Xi Chen) and C.Z.; project administration, W.G.; funding acquisition, W.G. All authors have read and agreed to the published version of the manuscript.

Funding: This research was funded by National Natural Science Foundation of Shaanxi Province, grant number: 2022JQ-433.

Data Availability Statement: Not applicable.

Acknowledgments: The authors thank for the special funding and equipment support of the visiting professor at North China University of Water Resources and Electric Power (No.4001-40734). The authors gratefully acknowledge the financial support provided by National Natural Science Foundation of Shaanxi province, China), grant number 2022JQ-433.

Conflicts of Interest: The authors declare no conflict of interest.

References

1. Chu, S.; Cui, Y.; Liu, N. The path towards sustainable energy. *Nat. Mater.* **2017**, *16*, 16–22. [CrossRef]
2. Stamenkovic, V.R.; Strmcnik, D.; Lopes, P.P.; Markovic, N.M. Energy and fuels from electrochemical interfaces. *Nat. Mater.* **2017**, *16*, 57–69. [CrossRef]
3. Ding, H.; Liu, H.F.; Chu, W.S.; Wu, C.Z.; Xie, Y. Structural transformation of heterogeneous materials for electrocatalytic oxygen evolution reaction. *Chem. Rev.* **2021**, *121*, 13174–13212. [CrossRef]
4. Wang, Y.; Li, J.; Wei, Z.D. Transition-metal-oxide-based catalysts for the oxygen reduction reaction. *J. Mater. Chem. A* **2018**, *6*, 8194–8209. [CrossRef]
5. Zhang, J.T.; Zhao, Z.H.; Xia, Z.H.; Dai, L.M. A metal-free bifunctional electrocatalyst for oxygen reduction and oxygen evolution reactions. *Nat. Nanotechnol.* **2015**, *10*, 444–452. [CrossRef]
6. Cook, T.R.; Dogutan, D.K.; Reece, S.Y.; Surendranath, Y.; Teets, T.S.; Nocera, D.G. Solar energy supply and storage for the legacy and nonlegacy worlds. *Chem. Rev.* **2010**, *110*, 6474–6502. [CrossRef]
7. Nie, Y.; Li, L.; Wei, Z.D. Recent advancements in Pt and Pt-free catalysts for oxygen reduction reaction. *Chem. Soc. Rev.* **2015**, *44*, 2168–2201. [CrossRef]
8. Reier, T.; Oezaslan, M.; Strasser, P. Electrocatalytic oxygen evolution reaction (OER) on Ru, Ir, and Pt catalysts: A comparative study of nanoparticles and bulk materials. *ACS Catal.* **2012**, *2*, 1765–1772. [CrossRef]
9. Wang, W.; Liu, E.S.; Hu, Y.C.; Jiao, L.; Kolla, P.; Liu, Y.C.; Tang, M.H.; Luo, J.; Sun, Q.; Chen, S.L.; et al. Understanding the ORR electrocatalysis on Co–Mn oxides. *J. Phys. Chem. C* **2021**, *125*, 25470–25477. [CrossRef]
10. Xu, Y.J.; Sumboja, A.; Zong, Y.; Darr, J.A. Bifunctionally active nanosized spinel cobalt nickel sulfides for sustainable secondary zinc–air batteries: Examining the effects of compositional tuning on OER and ORR activity. *Catal. Sci. Technol.* **2020**, *10*, 2173–2182. [CrossRef]
11. Ji, D.W.; Liu, C.H.; Yao, Y.H.; Luo, L.L.; Wang, W.C.; Chen, Z.D. Cerium substitution in $LaCoO_3$ perovskite oxide as bifunctional electrocatalysts for hydrogen and oxygen evolution reactions. *Nanoscale* **2021**, *13*, 9952–9959. [CrossRef]
12. Gu, X.-K.; Samira, S.; Nikolla, E. Oxygen sponges for electrocatalysis: Oxygen reduction/evolution on nonstoichiometric, mixed metal oxides. *Chem. Mater.* **2018**, *30*, 2860–2872. [CrossRef]
13. Patra, S.; Choudhary, R.; Roy, E.; Madhuri, R.; Sharma, P.K. Heteroatom-doped graphene 'Idli': A green and foody approach towards development of metal free bifunctional catalyst for rechargeable zinc-air battery. *Nano Energy* **2016**, *30*, 118–129. [CrossRef]
14. Zhao, Q.; Yan, Z.H.; Chen, C.C.; Chen, J. Spinels: Controlled preparation, oxygen reduction/evolution reaction application, and beyond. *Chem. Rev.* **2017**, *117*, 10121–10211. [CrossRef]

15. Li, C.; Han, X.P.; Cheng, F.Y.; Hu, Y.X.; Chen, C.C.; Chen, J. Phase and composition controllable synthesis of cobalt manganese spinel nanoparticles towards efficient oxygen electrocatalysis. *Nat. Commun.* **2015**, *6*, 1–8. [CrossRef]
16. Devaguptapu, S.V.; Hwang, S.; Karakalos, S.; Zhao, S.; Gupta, S.; Su, D.; Xu, H.; Wu, G. Morphology control of carbon-free spinel $NiCo_2O_4$ catalysts for enhanced bifunctional oxygen reduction and evolution in alkaline media. *ACS Appl. Mater. Interfaces* **2017**, *9*, 44567–44578. [CrossRef]
17. Liu, W.J.; Bao, J.; Xu, L.; Guan, M.L.; Wang, Z.L.; Qiu, J.X.; Huang, Y.P.; Xia, J.X.; Lei, Y.C.; Li, H.M. $NiCo_2O_4$ ultrathin nanosheets with oxygen vacancies as bifunctional electrocatalysts for Zn-air battery. *Appl. Surf. Sci.* **2019**, *478*, 552–559. [CrossRef]
18. Hirai, S.; Yagi, S.; Seno, A.; Fujioka, M.; Ohno, T.; Matsuda, T. Enhancement of the oxygen evolution reaction in Mn^{3+}-based electrocatalysts: Correlation between Jahn–Teller distortion and catalytic activity. *RSC Adv.* **2016**, *6*, 2019–2023. [CrossRef]
19. Xu, Y.J.; Sumboja, A.; Groves, A.; Ashton, T.; Zong, Y.; Darr, J.A. Enhancing bifunctional catalytic activity of cobalt–nickel sulfide spinel nanocatalysts through transition metal doping and its application in secondary zinc-air batteries. *RSC Adv.* **2020**, *10*, 41871–41882. [CrossRef]
20. An, L.; Huang, L.; Zhou, P.P.; Yin, J.; Liu, H.Y.; Xi, P.X. A self-standing high-performance hydrogen evolution electrode with nanostructured $NiCo_2O_4$/CuS heterostructures. *Adv. Funct. Mater.* **2015**, *25*, 6814–6822. [CrossRef]
21. Wang, L.M.; Liu, Q.F.; Ta, N.; Fan, H.F.; Wang, E.D. Multi-functional cerium modification to accelerate the oxygen reduction reaction of spinel Co_3O_4. *ChemistrySelect* **2021**, *6*, 3512–3518. [CrossRef]
22. Wang, X.-T.; Ouyang, T.; Wang, L.; Zhong, J.-H.; Liu, Z.-Q. Surface reorganization on electrochemically-induced Zn–Ni–Co spinel oxides for enhanced oxygen electrocatalysis. *Angew. Chem. Int. Ed.* **2020**, *132*, 6554–6561. [CrossRef]
23. Chutia, B.; Hussain, N.; Puzari, P.; Jampaiah, D.; Bhargava, S.K.; Matus, E.V.; Ismagilov, I.Z.; Kerzhentsev, M.; Bharali, P. Unraveling the role of CeO_2 in stabilization of multivalent Mn species on α-MnO_2/Mn_3O_4/CeO_2/C surface for enhanced electrocatalysis. *Energy Fuels* **2021**, *35*, 10756–10769. [CrossRef]
24. Li, J.B.; Shu, C.Z.; Hu, A.J.; Ran, Z.Q.; Li, M.L.; Zheng, R.X.; Long, J.P. Tuning oxygen non-stoichiometric surface via defect engineering to promote the catalysis activity of Co_3O_4 in Li-O_2 batteries. *Chem. Eng. J.* **2020**, *381*, 122678. [CrossRef]
25. Liu, Y.; Ma, C.; Zhang, Q.H.; Wang, W.; Pan, P.F.; Gu, L.; Xu, D.D.; Bao, J.C.; Dai, Z.H. 2D electron gas and oxygen vacancy induced high oxygen evolution performances for advanced Co_3O_4/CeO_2 nanohybrids. *Adv. Mater.* **2019**, *31*, 1900062. [CrossRef]
26. Xu, H.J.; Wang, B.K.; Shan, C.F.; Xi, P.X.; Liu, W.S.; Tang, Y. Ce-doped NiFe-layered double hydroxide ultrathin nanosheets/nanocarbon hierarchical nanocomposite as an efficient oxygen evolution catalyst. *ACS Appl. Mater. Interfaces* **2018**, *10*, 6336–6345. [CrossRef]
27. Liu, K.; Huang, X.B.; Wang, H.Y.; Li, F.Z.; Tang, Y.G.; Li, J.S.; Shao, M.H. Co_3O_4–CeO_2/C as a highly active electrocatalyst for oxygen reduction reaction in Al-air batteries. *ACS Appl. Mater. Interfaces* **2016**, *8*, 34422–34430. [CrossRef]
28. Lee, J.; Ryou, Y.S.; Chan, X.J.; Kim, T.J.; Kim, D.H. How Pt interacts with CeO_2 under the reducing and oxidizing environments at elevated temperature: The origin of improved thermal stability of Pt/CeO_2 compared to CeO_2. *J. Phys. Chem. C* **2016**, *120*, 25870–25879. [CrossRef]
29. Iliev, M.N.; Padhan, P.; Gupta, A. Temperature-dependent Raman study of multiferroic Bi_2NiMnO_6 thin films. *Phys. Rev. B* **2008**, *77*, 172303. [CrossRef]
30. Hu, Z.X.; Zhou, X.X.; Lu, Y.; Jv, R.M.; Liu, Y.; Li, N.; Chen, S.W. $CoMn_2O_4$ doped reduced graphene oxide as an effective cathodic electrocatalyst for ORR in microbial fuel cells. *Electrochim. Acta* **2019**, *296*, 214–223. [CrossRef]
31. Xu, J.; Gao, P.; Zhao, T. Non-precious Co_3O_4 nano-rod electrocatalyst for oxygen reduction reaction in anion-exchange membrane fuel cells. *Energy Environ. Sci.* **2012**, *5*, 5333–5339. [CrossRef]
32. Dong, C.; Qu, Z.P.; Qin, Y.; Fu, Q.; Sun, H.C.; Duan, X.X. Revealing the highly catalytic performance of spinel $CoMn_2O_4$ for toluene oxidation: Involvement and replenishment of oxygen species using in situ designed-TP techniques. *ACS Catal.* **2019**, *9*, 6698–6710. [CrossRef]
33. Liu, B.; Li, C.M.; Zhang, G.Q.; Yao, X.S.; Chuang, S.S.C.; Li, Z. Oxygen vacancy promoting dimethyl carbonate synthesis from CO_2 and methanol over Zr-doped CeO_2 nanorods. *ACS Catal.* **2018**, *8*, 10446–10456. [CrossRef]
34. Zhang, S.; Xia, Z.M.; Zou, Y.; Cao, F.X.; Liu, Y.X.; Ma, Y.Y.; Qu, Y.Q. Interfacial frustrated Lewis pairs of CeO_2 activate CO_2 for selective tandem transformation of olefins and CO_2 into cyclic carbonates. *J. Am. Chem. Soc.* **2019**, *141*, 11353–11357. [CrossRef] [PubMed]
35. Qiu, C.; Qian, K.; Yu, J.; Sun, M.Z.; Cao, S.F.; Gao, J.Q.; Yu, R.X.; Fang, L.Z.; Yao, Y.W.; Lu, X.Q.; et al. MOF-transformed In_2O_3-x@C nanocorn electrocatalyst for efficient CO_2 reduction to HCOOH. *Nano-Micro Lett.* **2022**, *14*, 167. [CrossRef] [PubMed]
36. Ma, T.; Li, C.; Chen, X.; Cheng, F.Y.; Chen, J. Spinel cobalt–manganese oxide supported on non-oxidized carbon nanotubes as a highly efficient oxygen reduction/evolution electrocatalyst. *Inorg. Chem. Front.* **2017**, *4*, 1628–1633.
37. Chen, J.J.; Zhou, N.; Wang, H.Y.; Peng, Z.G.; Li, H.Y.; Tang, Y.G.; Liu, K. Synergistically enhanced oxygen reduction activity of MnO_x-CeO_2/ketjenblack composites. *Chem. Commun.* **2015**, *51*, 10123–10126. [CrossRef]
38. Su, H.; Wang, X.T.; Hu, J.X.; Ouyang, T.; Xiao, K.; Liu, Z.Q. Co-Mn spinel supported self-catalysis induced N-doped carbon nanotubes with high efficiency electron transport channels for zinc-air batteries. *J. Mater. Chem. A* **2019**, *7*, 22307–22313. [CrossRef]
39. Han, X.P.; Wu, X.Y.; Zhong, C.; Deng, Y.D.; Zhao, N.Q.; Hu, W.B. $NiCo_2S_4$ nanocrystals anchored on nitrogen-doped carbon nanotubes as a highly efficient bifunctional electrocatalyst for rechargeable zinc-air batteries. *Nano Energy* **2017**, *31*, 541–550. [CrossRef]

40. Gou, W.Y.; Zhang, M.K.; Zou, Y.; Zhou, X.M.; Qu, Y.Q. Iridium-chromium oxide nanowires as highly performed OER catalysts in acidic media. *ChemCatChem* **2019**, *11*, 6008–6014. [CrossRef]
41. Chang, K.; Tran, D.T.; Wang, J.Q.; Kim, N.H.; Lee, J.H. A 3D hierarchical network derived from 2D Fe-doped NiSe nanosheets/carbon nanotubes with enhanced OER performance for overall water splitting. *J. Mater. Chem. A* **2022**, *10*, 3102–3111. [CrossRef]
42. Singh, T.I.; Maibam, A.; Cha, D.C.; Yoo, S.; Babarao, R.; Lee, S.U.; Lee, S. High-alkaline water-splitting activity of mesoporous 3D heterostructures: An amorphous-shell@crystalline-core nano-assembly of Co-Ni-Phosphate ultrathin-nanosheets and V- doped Cobalt-Nitride nanowires. *Adv. Sci.* **2022**, *9*, 2201311. [CrossRef] [PubMed]